

Buckling of spherical shells adhering onto a rigid substrate

S. Komura^a, K. Tamura, and T. Kato

Department of Chemistry, Faculty of Science, Tokyo Metropolitan University, Tokyo 192-0397, Japan

Received 28 July 2005 / Received in final form 2 October 2005

Published online 15 November 2005 – © EDP Sciences, Società Italiana di Fisica, Springer-Verlag 2005

Abstract. Deformation of a spherical shell adhering onto a rigid substrate due to van der Waals attractive interaction is investigated by means of numerical minimization (conjugate gradient method) of the sum of the elastic and adhesion energies. The conformation of the deformed shell is governed by two dimensionless parameters, *i.e.*, C_s/ϵ and C_b/ϵ where C_s and C_b are respectively the stretching and the bending constants, and ϵ is the depth of the van der Waals potential between the shell and substrate. Four different regimes of deformation are characterized as these parameters are systematically varied: (i) small deformation regime, (ii) disk formation regime, (iii) isotropic buckling regime, and (iv) anisotropic buckling regime. By measuring the various quantities of the deformed shells, we find that both discontinuous and continuous buckling transitions occur for large and small C_s/ϵ , respectively. This behavior of the buckling transition is analogous to van der Waals liquids or gels, and we have numerically determined the associated critical point. Scaling arguments are employed to explain the adhesion induced buckling transition, *i.e.*, from the disk formation regime to the isotropic buckling regime. We show that the buckling transition takes place when the indentation length exceeds the effective shell thickness which is determined from the elastic constants. This prediction is in good agreement with our numerical results. Moreover, the ratio between the indentation length and its thickness at the transition point provides a constant number (2–3) independent of the shell size. This universal number is observed in various experimental systems ranging from nanoscale to macroscale. In particular, our results agree well with the recent compression experiment using microcapsules.

PACS. 46.32.+x Static buckling and instability – 68.35.Np Adhesion – 81.05.Tp Fullerenes and related materials

1 Introduction

1.1 Elastic sheets

Investigations of structures and properties of thin elastic sheets are important for both practical and industrial reasons. Their applications in our daily life are such as cans, houses, domes, bridges, ships, planes, etc. When elastic sheets are subjected to a large external force, they lose their shape and buckle at a critical force as we often experience. In engineering of safety structures, it is desired to increase the buckling threshold as large as possible. As discussed below, one of the characteristic features of thin elastic sheets is that the energy required for stretching is very large compared to that for bending. Hence pure bending deformations without any stretching are preferred in general.

In recent years, considerable attentions have been paid to thin materials which exhibit elastic behaviors at either microscopic or mesoscopic scales. For example, the conformation of two-dimensional sheets of graphitic oxide

was investigated by electron microscopy and other techniques [1,2]. A sheet of graphitic oxide is flat on average due to its finite in-plane shear elasticity in spite of out-of-plane thermal fluctuations [3]. For a two-dimensional polymer network (polymerized silane monolayer) at the air-water interface, a buckling phenomenon was observed by X-ray scattering [4]. The other group found a continuous buckling transition for a solid Langmuir monolayer composed of phospholipid molecules deposited on the surface of formamide [5,6]. A more complex elastic sheet can be found in a cell membrane skeleton called “cytoskeleton” which is a two-dimensional triangulated network consisting mainly of actin and spectrin molecules. Such kind of biological membranes take locally rough but globally flat configuration even in the presence of thermal fluctuations [7]. Deflection of a cell membrane under a localized force or torque was discussed theoretically [8].

From the theoretical point of view, the properties of stretching ridges in a crumpled elastic sheet has been studied intensively during the past decade. The crumpling of a thin sheet can be understood as the condensation of elastic energy into a network of ridges [9,10]. The problem of ridges was initiated by Witten and Li who realized

^a e-mail: komura@comp.metro-u.ac.jp

that the elastic energy of a ridge scales as $X^{1/3}$, where X is the length of the ridge [11, 12]. Lobkovsky re-derived the same ridge scaling relation by performing a boundary layer analysis of the Föppl-von Kármán (FvK) equations for plates [13, 14]. Note that the term “plate” means a thin sheet of elastic material of constant thickness which is plane in its rest state. More recently, DiDonna and Witten investigated the compression and buckling of elastic ridges, and showed that the energy required to buckle it is nearly a constant fraction (20%) of the total ridge elastic energy [15, 16]. In fact, this explains why crumpled sheets are qualitatively stronger than smoothly bent sheets [17].

In general, the highly nonlinear FvK equations are very difficult to solve because they involve two types of deformation (stretching and bending) with energies of different orders of magnitude [18]. Nevertheless, the FvK equations have been the subject of renewed interest in the context of developable cone (d-cone) singularities. Surprisingly, a geometry of a d-cone is one of the solutions to the complicated FvK equations [19]. Some scaling relations for the core size of the d-cone singularity was obtained in references [19, 20]. Being inspired by these theoretical predictions, several macroscopic experiments were performed to investigate the shape, response, and stability of the d-cone singularities [21–23].

Other than the d-cone geometry, Audoly *et al.* predicted various buckling modes of a long rectangular elastic plate subjected to the applied longitudinal and transverse compressions [24–26]. Reference [27] reports the case in which a plate was initially bent in one direction into a cylindrical arch, and then deformed in the other direction. Later the core energy of the d-cone singularity was measured by piercing the plate around the singularity [28]. More recently, wrinkling of an elastic sheet was discussed by Cerda and Mahadevan [29, 30].

1.2 Shells

It should be stressed, however, that most of the above works are concerned with elastic sheets which are flat in the undeformed state, while less attention has been paid for the properties of initially curved elastic sheets, *i.e.*, *shells*. Moreover, the FvK equations are valid only for a plane geometry, and a covariant generalization for any curved shell is still lacking. In particular, a shell exhibits a peculiar elastic feature because the strain tensor is proportional to the first power of the out-of-plane displacement (see Sect. 2 for the details), and the shell cannot be bent without being stretched [18]. For a plate, typical stretching and bending energies per unit area scale as

$$E_s \sim Yh\zeta^4/\ell^4, \quad E_b \sim Yh^3\zeta^2/\ell^4, \quad (1)$$

respectively, where Y is the Young’s modulus, h the thickness of the elastic sheet, ζ the magnitude of the out-of-plane displacement, and ℓ is a typical length scale. Since the ratio between the two energies is $E_s/E_b \sim (\zeta/h)^2$, the stretching energy can be neglected in the limit of $\zeta \ll h$.

Conversely, the stretching energy becomes dominant as soon as the displacement ζ is larger than the thickness h . For a spherical shell of radius R , on the other hand, the respective energies are given by

$$E_s \sim Yh\zeta^2/R^2, \quad E_b \sim Yh^3\zeta^2/R^4. \quad (2)$$

Then the similar ratio for a shell becomes $E_s/E_b \sim (R/h)^2$, which is typically very large. Hence the bending deformation inevitably accompanies the stretching deformation for a shell. In contrast to the case of a plate, this fact does not depend on the ratio ζ/h of the shell.

As an example of this interplay between the stretching and bending modes, the shape fluctuations and the stability of a cylindrical shell (polymerized vesicle) was studied before [31]. It was shown that the intrinsic curvature of the shell leads to an enhanced coupling between the two elastic modes, and act to suppress the shape fluctuations on large scales. A similar analysis for a spherical shell revealed that such a suppression effect is more pronounced when shells are closed [32–34]. The enhanced stability of shells is crucial for constructing large structures such as domes or bridges.

There are some experimental works which deal with the deformation of spherical shells. By using actin-coated vesicles [35], a buckling instability was observed when a large localized force is applied [36]. At macroscopic level, on the other hand, contact and compression problem of a ping-pong ball was investigated by Pauchard and Rica [37, 38]. The same author reported that buckling instability occurs during the drying of sessile drops of polymer solution [39]. Similar phenomena were found also by using droplets of colloidal suspensions [40, 41]. Rather recently, elastic properties of polyelectrolyte capsules [42, 43] are studied by AFM and reflection interference contrast microscopy [44–46]. The details of these experimental works will be discussed in Section 6 in order to compare with our results.

1.3 Adhesion

Among various types of deformation, adhesion onto a substrate due to van der Waals interaction plays an important role especially in the field of nanotechnology. For example, the electric transport through carbon nanotubes is studied after their deposition on a substrate with which they interact each other. Unfortunately, it is known that the resistivity of the nanotube is affected by its elastic deformation. Since there is little control over the alignment and the shape of adsorbed nanotubes, it is crucial to know how they deform on the substrate. The deformations of multi-walled nanotubes on a rigid substrate was observed and investigated using atomic force microscopy (AFM) [47] and molecular-mechanics simulations [48]. Later a collapse of a nanotube section due to the surface interaction was observed by using AFM [49]. More recently, a systematic numerical study on the deformation of an elastic nanotube adhering onto a substrate was reported by the present authors [50]. However, we stress here that the adhesion and

contact problem of a spherically closed shell has not yet been investigated in detail. One exception is reference [51] in which some scaling arguments for the deformation and mechanical stability of fullerene-like hollow nanoparticles were given by employing the shell theory. It was shown that van der Waals interactions between a substrate and adhering nanoparticles can cause considerable deformations. Such an effect is important for tribological applications of fullerene-like nanoparticles [52].

1.4 Present work

In this paper, we investigate both numerically and theoretically the deformation and the stability of a spherically closed shell adhering onto a rigid substrate due to van der Waals attractive interaction. Some of the results have been published elsewhere [53]. To consider the shell adhesion, we propose a discretized model in which the equilibrium configuration of the shell is determined according to the competition among three energies, *i.e.*, stretching, bending, and van der Waals energies. The total energy is numerically minimized by using the conjugate gradient method. The effects of thermal fluctuations are not taken into account in the present model. One of our main findings is the fact that the adhesion causes a buckling transition of a spherical shell as either the elastic properties and/or the strength of adhesion is varied. More interestingly, our systematic study revealed that the buckling transition can be either continuous or discontinuous depending on the elastic properties of the shell such as the stretching or bending constants. We identify a special point which is analogous to the critical point for van der Waals fluids which exhibits liquid-gas coexistence. We have also performed the scaling analysis to explain the adhesion induced buckling of spherical shells. Once the buckling occurs, a polygonal structure consisting of ridges and d-cones is created when the adhesion is strong enough.

Our work can be regarded in part as a contact problem of spherical shells. For two elastic bodies, their contact problem under an applied load was solved by Hertz long time ago [18,54]. After ninety years, the Hertz's solution was extended to take into account the influence of adhesion energy [55,56]. In the presence of the adhesion energy, the apparent load acting between the two elastic bodies is larger than the applied load. In contrast to the contact problem of elastic bodies, there are few works which deal with the corresponding problem of elastic shells.

This paper is constructed as follows. In the next section, we briefly review the framework of the continuum elasticity theory for shells. In Section 3, we describe our model for shells adhering onto a rigid substrate. We also explain the numerical method to calculate the equilibrium structure. Then we present the obtained results together with various quantitative analyses of the shell structures in Section 4. In Section 5, we provide some scaling arguments concerning the deformation of shells, and compare them with our numerical results. Finally, the paper is closed with discussions in Section 6 where we compare our results with several previous experiments.

2 Shell theory

In this section, we describe the continuum version of the shell theory [18]. We collect some formulas from differential geometry which is the most appropriate formalism for the classical theory of elastic shells. See reference [57] for a further treatment.

One can, in general, parameterize a two-dimensional thin sheet in three-dimensional space by two real inner coordinates $\mathbf{s} = (s^1, s^2)$. The shape of the sheet is then described by a three-dimensional vector $\mathbf{r} = \mathbf{r}(\mathbf{s})$. At each point on the sheet, there are two tangent vectors $\mathbf{r}_i = \partial\mathbf{r}/\partial s^i$ with $i = 1, 2$. The outward unit normal vector $\hat{\mathbf{n}}$ is perpendicular to these tangent vectors, *i.e.*,

$$\hat{\mathbf{n}} = \frac{\mathbf{r}_1 \times \mathbf{r}_2}{|\mathbf{r}_1 \times \mathbf{r}_2|}. \quad (3)$$

All properties related to the intrinsic geometry of the sheet are expressed in terms of the metric tensor (or the fundamental tensor) defined by

$$g_{ij} = \mathbf{r}_i \cdot \mathbf{r}_j. \quad (4)$$

Two important quantities are the determinant and the inverse of the metric tensor which will be denoted by

$$g = \det(g_{ij}), \quad (5)$$

and

$$g^{ij} = (g_{ij})^{-1}, \quad (6)$$

respectively. In addition, one has to consider the (extrinsic) curvature tensor (or the second fundamental tensor) given by

$$h_{ij} = \hat{\mathbf{n}} \cdot \partial_j \mathbf{r}_i = -\hat{\mathbf{n}}_i \cdot \mathbf{r}_j, \quad (7)$$

with $\partial_j \mathbf{r}_i = \partial^2 \mathbf{r} / \partial s^i \partial s^j$. Note that a surface is uniquely characterized by its metric tensor g_{ij} and the curvature tensor h_{ij} .

Let us define the (undeformed) reference state as $\mathbf{r} = \mathbf{R}$. Here and below, we shall use capital letters in order to distinguish quantities in the reference state from the corresponding quantities in the deformed state. Thus, \mathbf{R}_i , $\hat{\mathbf{N}}_i$, G_{ij} , H_{ij} represent the tangent and normal vectors, the metric and the curvature tensors in the reference state, respectively. If the sheet is stretched, the distance between two neighboring points in the sheet is changed. This change can be expressed in terms of the strain tensor u_{ij} defined by [58]

$$u_{ij} = \frac{1}{2}(g_{ij} - G_{ij}). \quad (8)$$

The mixed strain tensor is obtained by raising one of the indices according to

$$u_i{}^j = u_{ik} g^{kj}. \quad (9)$$

Here and below, we use Einstein's summation convention and sum over all indices which appear twice. Likewise, the mixed bending tensor

$$b_{ij} = h_{ij} - H_{ij} \quad (10)$$

is taken as a measure for the bending deformation. Note that this choice is not unique and alternative definitions are possible. We will discuss this point later.

Consider a deformation of a shell which can be parametrized by

$$\mathbf{r} = \mathbf{R} + u^i \mathbf{R}_i + \zeta \hat{\mathbf{N}}. \quad (11)$$

The contravariant vector u^i ($i = 1, 2$) represents lateral (in-plane) displacement field and ζ represents the transverse (out-of-plane) displacement field. Both strain tensor and bending tensor can be expressed in terms of the components of these displacement fields. Up to first order in the displacement $\mathbf{r} - \mathbf{R}$, the strain tensor turns out to be

$$u_{ij} \approx \frac{1}{2}(D_i u_j + D_j u_i) - \zeta H_{ij}, \quad (12)$$

where the covariant components of the lateral displacement fields are given by $u_j = A^i g_{ij}$, and the covariant derivative D_i is defined by

$$D_i u_j = \partial_i u_j - \Gamma_{ij}^k u_k, \quad (13)$$

with the Christoffel symbol

$$\Gamma_{ik}^j = \frac{1}{2} G^{jl} (\partial_i G_{kl} + \partial_k G_{il} - \partial_l G_{ik}), \quad (14)$$

and $\partial_i = \partial/\partial s^i$. In a similar manner, the linear approximation for b_{ij} leads to

$$b_{ij} \approx D_i D_j \zeta - \zeta H_i^k H_{jk} + H_{ik} (D_j u^k) + H_{jk} (D_i u^k) + u^k (D_j H_{ik}). \quad (15)$$

In the Donnell-Mushtari-Vlasov approximation [57], the bending tensor is simplified to

$$b_{ij} \approx D_i D_j \zeta. \quad (16)$$

As mentioned, we have defined the bending tensor b_{ij} in terms of the difference between the covariant components of the curvature tensors in the deformed and the initial state (see Eq. (10)). If we had selected, for instance, the difference between the mixed components, $\tilde{b}_i^j = h_i^j - H_i^j$, or the contravariant components, $\bar{b}^{ij} = h^{ij} - H^{ij}$, the results would be different. This fact is of great importance to the shell theory, although the term $D_i D_j \zeta$ in equation (15) is not affected by the different measures of bending. From a purely formal point of view, we may take any measure of strain and bending from which the original measures can be recovered. There is, in fact, no physical ground for selecting one of the bending tensors.

Let σ^{ij} be the components of three-dimensional stress in normal coordinates and η^{ij} corresponding components of three-dimensional strain. For a bulk material that obeys Hooke's law, the stress tensor is given in terms of the strain tensor by [57]

$$\sigma^{ij} = \frac{Y}{1+\nu} \left(\eta^{ij} + \frac{\nu}{1-2\nu} g^{ij} \eta_k^k \right), \quad (17)$$

where Y and ν are the (three-dimensional) Young's modulus and the Poisson's ratio, respectively. Then the elastic energy density is given by

$$f_e = \frac{1}{2} \int_{-h/2}^{h/2} \sigma^{ij} \eta_{ij} \left(\frac{A}{G} \right)^{1/2} dz, \quad (18)$$

where h is the thickness of the shell and

$$A = \frac{1}{G} [\det(G_{ij} - H_{ij} z)]^2. \quad (19)$$

According to the shell theory, f_e can be expressed in terms of u_{ij} and b_{ij} by constructing the possible invariants with respect to coordinate transformations. Within the linear elasticity, the deformation energy of an isotropic shell is given by [57]

$$f_e = \frac{Yh}{2(1-\nu^2)} [\nu u_i^i u_j^j + (1-\nu) u_i^j u_j^i] + \frac{Yh^3}{24(1-\nu^2)} [\nu b_i^i b_j^j + (1-\nu) b_i^j b_j^i]. \quad (20)$$

From the principle of virtual work, we have

$$\delta W = \frac{\partial W}{\partial u_{ij}} \delta u_{ij} + \frac{\partial W}{\partial b_{ij}} \delta b_{ij}, \quad (21)$$

where

$$\frac{\partial W}{\partial u_{ij}} = N^{ij}, \quad \frac{\partial W}{\partial b_{ij}} = M^{ij} \quad (22)$$

are effective membrane stress tensor and effective moment tensor, respectively. Then we can derive the *constitutive equations* for shells:

$$N^{ij} = \frac{Yh}{(1-\nu^2)} [\nu g^{ij} u_k^k + (1-\nu) u^{ij}], \quad (23)$$

$$M^{ij} = \frac{Yh^3}{24(1-\nu^2)} [\nu g^{ij} b_k^k + (1-\nu) b^{ij}]. \quad (24)$$

Using the identity $\det(b_i^j) = \frac{1}{2}(b_i^i b_j^j - b_i^j b_j^i)$, one can rewrite the last two terms in equation (20) as

$$f_e = \frac{Yh}{2(1-\nu^2)} [\nu u_i^i u_j^j + (1-\nu) u_i^j u_j^i] + \frac{\kappa}{2} b_i^i b_j^j + \bar{\kappa} \det(b_i^j), \quad (25)$$

with

$$\kappa = \frac{Yh^3}{12(1-\nu^2)}, \quad (26)$$

$$\bar{\kappa} = -\frac{Yh^3}{12(1+\nu)}. \quad (27)$$

Since b_{ij} has been defined by the difference between two curvature tensors, it has to satisfy certain compatibility conditions in order to be itself a curvature tensor. In such case, κ and $\bar{\kappa}$ are called bending rigidity and Gaussian curvature modulus, respectively. Hence, in general, the Gauss-Bonnet theorem will not apply to equation (25). For a planar reference state, however, the Gauss-Bonnet theorem applies.

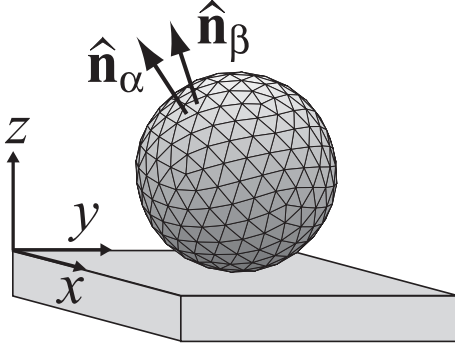


Fig. 1. Beads and springs model for an elastic spherical shell adhering onto a substrate. $\hat{\mathbf{n}}_{\alpha(\beta)}$ is the unit normal vector of the triangle $\alpha(\beta)$.

3 Model

Consider an elastic spherical shell interacting with a rigid substrate as shown in Figure 1. The normal directions to the substrate is taken as the z -axis, whereas the substrate spans the xy -plane. In the discretized model, the configuration of the shell is represented by a triangular mesh as a simplest approximation for a two-dimensional elastic material. In the absence of adhesion, the initial configuration of the shell is taken to be spherical. The initial configuration is constructed by the Delaunay triangulation of the spherical surface [59,60]. Starting from an icosahedron as the original network, we add new points on each triangle followed by a subsequent rescaling of all bonds to the desired length [61,62]. Although there are always 12 grid points which have five neighbors, this procedure ensures that most of grid points have six neighbors and each bond has approximately the same length. The singularity associated with the fivefold symmetry will be discussed later in Section 6. In the present work, we studied shells consisting of $N = 10 \times 3^k + 2$ grid points with $k = 1, \dots, 5$. The number of triangles is $f = 2N - 4$ while the number of bonds is $f = 3N - 6$. These quantities certainly satisfy the Euler's theorem; $N + f - e = 2$. In the next section, we mainly present the results for $k = 4$, *i.e.*, $N = 812$. The size effect will be separately discussed there. Hereafter we associate all the grid points and bonds with beads and springs, respectively.

To describe the deformation of an elastic shell, both the stretching and the bending energies should be taken into account [18,57]. Following the model of membranes with crystalline order [63], or crushed elastic manifolds [9], the discretized stretching energy is given by the sum over Hooke's law of each spring:

$$E_s = \sum_n \frac{1}{2} C_s \left(\frac{L_n - L_0}{L_0} \right)^2. \quad (28)$$

Here C_s is the stretching (spring) constant, L_n is the length of spring n , and L_0 is the natural length of the spring (or the lattice constant) taken here as a constant. On the other hand, the discretized bending energy is taken

into account by using the model of polymerized membranes with a finite bending constant [9,62–65];

$$E_b = \sum_{\langle \alpha\beta \rangle} \frac{1}{2} C_b |\hat{\mathbf{n}}_\alpha - \hat{\mathbf{n}}_\beta|^2, \quad (29)$$

where C_b is the bending constant, $\hat{\mathbf{n}}_{\alpha(\beta)}$ is the unit normal vector of triangle $\alpha(\beta)$, and the sum is taken over each pair of triangles which share a common edge. The bending constant C_b plays the role of a Heisenberg exchange coupling between neighboring normals. We note here that both C_s and C_b have the dimension of energy. The comparison between the continuum elasticity theory and these discretized elastic energies will be discussed later in Section 5.

To calculate the adhesion energy of the shell, we consider a generalized Lennard-Jones type interaction that is acting between each of the bead and the substrate:

$$W = \sum_i \frac{2^{8/3}}{3} \epsilon \left[\left(\frac{\sigma}{z_i} \right)^{12} - \left(\frac{\sigma}{z_i} \right)^3 \right], \quad (30)$$

where z_i is the height of bead i from the substrate, and the sum is taken over all the beads. When the adhesion energy of bead i is plotted against the distance z_i , the depth of the energy minimum is given by ϵ , and the distance corresponding to this minimum is $2^{2/9}\sigma$. The first repulsive term in equation (30) is responsible for the excluded volume interaction which prevents the beads from penetrating into the substrate. The power of this repulsive potential should not necessarily be 12, and a lower power such as 9 can be used as well. For our numerical calculations, it is more suitable to employ a stronger repulsive potential.

The second term represents the long-ranged attractive interaction between the beads and the substrate. The inverse cubic dependence of the above potential is briefly explained below [56,66]. The van der Waals attractive interaction between two atoms is generally given by the form

$$v(r) = -\frac{C}{r^6}, \quad (31)$$

where C is a constant depending on the physical origin of the attraction, and r is the distance between the two atoms. The simplest approach to obtain the interaction between an atom and a macroscopic body such as a substrate is to sum up the interactions between all pairs of atoms [56,66]. We consider a case where a single atom is placed at a distance D from a semi-infinite medium of density ρ . Then the total interaction energy is given by

$$w(D) = -\frac{2\pi\rho C}{12D^3}, \quad (32)$$

which gives rise to the inverse cubic dependence of the potential.

The total energy

$$E_{\text{tot}} = E_s + E_b + W \quad (33)$$

Table 1. The numerically obtained values of the critical point $(C_s/\epsilon)_c$, $(C_b/\epsilon)_c$, $(H/R)_c$ for the sizes $N = 92, 272, 812$, and 2432. We also list the values of the input parameters L_0/σ , R/σ , and R/L_0 . The values of $(h/R)_c$ at the critical point are calculated by using equation (46). $(H/h)_c$ is the ratio between $(H/R)_c$ and $(h/R)_c$. These numbers are almost independent of N .

N	L_0/σ	R/σ	R/L_0	$(C_s/\epsilon)_c$	$(C_b/\epsilon)_c$	$(H/R)_c$	$(h/R)_c$	$(H/h)_c$
92	0.1	0.25	2.5	5	0.35	1	0.29	3.4
272	0.1	0.43	4.3	80	1.5	0.26	0.089	2.9
812	0.1	0.75	7.5	210	6.1	0.18	0.064	2.8
2432	0.1	1.3	13	500	22	0.13	0.046	2.8

is numerically minimized using the conjugate gradient method [67]. Like most methods of multidimensional minimization, it is performed as a series of one-dimensional minimizations. For this purpose, a series of noninterfering, conjugate directions are constructed. As a result, minimization along one direction does not disturb the minimization in the other conjugate directions. Hereafter all the energies and the lengths are respectively scaled by ϵ and σ which characterize the shape of adhesion interaction in equation (30). There are three independent dimensionless parameters in the model, *i.e.*, C_s/ϵ , C_b/ϵ , and L_0/σ . In the present study, we have mainly varied C_s/ϵ and C_b/ϵ , whereas the other parameters are fixed. The scaled natural length of each bond L_0/σ is chosen such that the initial spherical configuration of the shell does not store any stretching energy E_s , and its value is roughly $L_0/\sigma \approx 0.1$. (Notice that not all the bonds have exactly the same natural length because of the singularity associated with the fivefold symmetry.) For $N = 812$, the scaled radius of the undeformed shell is $R/\sigma \approx 0.75$ (see Tab. 1). We note that the bending energy is inherent even in the undeformed spherical shell since the spontaneous curvature is not included in the present calculation. This assumption is justified such as for fullerene balls. (See also discussion in Sect. 6 concerning the spontaneous curvature of shells.)

In our model, the effect of thermal fluctuation is not included. Hence our calculation corresponds to the zero-temperature numerical simulation. Since the excluded volume effect of the surface is not included, we are dealing with “phantom” shells. As we shall see later, the neglect of self-avoidance effect is justified for most of the moderate deformations even when the buckling takes place. Self-avoidance can be crucial such as when the shell collapses due to a large negative pressure [51,62,68].

4 Results

In this section, we collect and present our numerical results which are analyzed by various quantitative methods. Some of them have been already published elsewhere [53]. We mainly discuss the results from the size $N = 812$. The size dependence is discussed in Section 4.6.

4.1 Configurations

By looking at various equilibrium configurations of the deformed shells, we find that there are basically four qualitatively distinct types of deformation as the combination

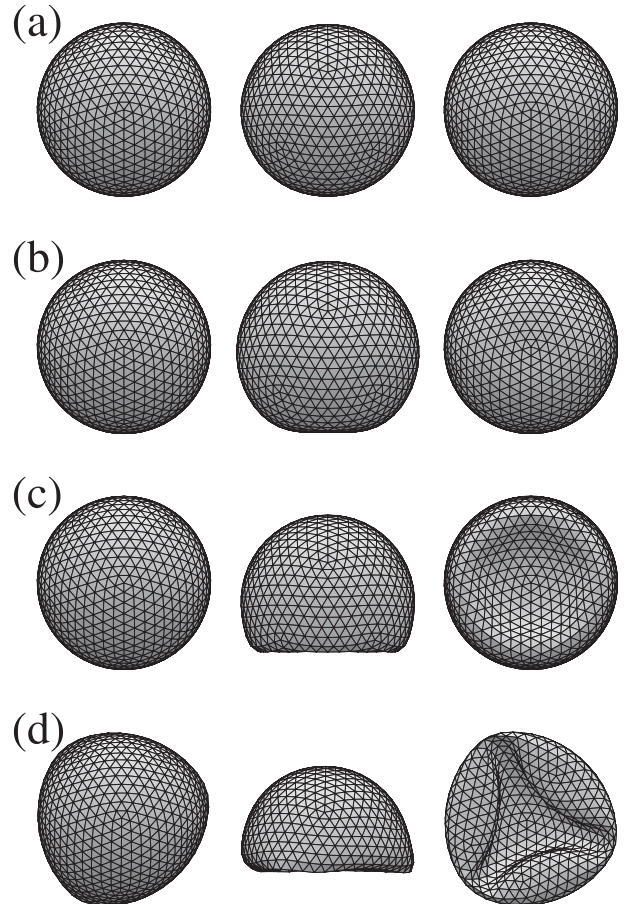


Fig. 2. Top, side and bottom views of the equilibrated configurations of adhering spherical shells when the sets of the scaled elastic constants $(C_s/\epsilon, C_b/\epsilon)$ are (a) (1000, 1000), (b) (150, 9), (c) (150, 2), and (d) (100, 1).

of C_s/ϵ and C_b/ϵ is systematically varied. Typical examples for these cases are shown in Figure 2 from (a) to (d). For a given parameter set, the deformed shell is seen from top, side, and bottom with respect to the substrate. Figure 2a ($C_s/\epsilon = 1000$, $C_b/\epsilon = 1000$) corresponds to the situation when both of the elastic constants are very large compared to the adhesion energy. Here the shell hardly deforms in spite of the adhesion, and keeps its spherical shape (“*small deformation regime*”). This means that the effect of adhesion is practically irrelevant.

When both of the elastic constants are simultaneously decreased, we observe the case Figure 2b ($C_s/\epsilon = 150$,

$C_b/\epsilon = 9$). Here a flat contact disk develops at the bottom of the shell as can be observed from the side view (“*disk formation regime*”). The area of the contact disk increases as the adhesion energy ϵ becomes larger. The formation of a flat contact disk is reminiscent of the flattening of elastic tubes along the contact region [50].

Keeping the value of C_s/ϵ while decreasing the bending constant C_b/ϵ results in the buckling of the shell as illustrated in Figure 2c ($C_s/\epsilon = 150$, $C_b/\epsilon = 2$). For such a buckled configuration, both the stretching and the bending energies are localized at a narrow “bending strip” of contact. The competition between the two energies determines its width, which will be discussed later in Section 5 within the scaling argument. The bending strip is formed in a circular shape, and the whole configuration of the shell is almost isotropic in the xy -direction (“*isotropic buckling regime*”). The buckled region of the shell is bent inward, but it does not violate the excluded volume effect.

In the case of Figure 2d ($C_s/\epsilon = 100$, $C_b/\epsilon = 1$), it becomes energetically favorable for the buckled region to create a polygonal structure composed of a number of ridges joined by the d-cones. In contrast to the isotropic buckling in Figure 2c, the shell buckles in an anisotropic manner (“*anisotropic buckling regime*”). To characterize such a buckled shape is related to the problem of post-buckling. The number of ridges is dependent on the van der Waals adhesive energy, which will be argued below. We remind here that neither isotropic nor anisotropic buckling has never been observed for elastic tubes [50].

In order to see the sequence of the systematic deformation more clearly, we fixed the stretching constant to $C_s/\epsilon = 100$ and varied the bending constant C_b/ϵ from 50 to 1.1. The top, side and bottom views of the equilibrium configurations are arranged in Figure 3. Figure 3a belongs to the small deformation regime, (b) to the disk formation regime, (c) and (d) to the isotropic buckling regime, and (e) and (f) to the anisotropic buckling regime, respectively. It is remarkable that, in the anisotropic buckling regime, only a slight change in the value of C_b/ϵ causes a big difference in the final configuration, namely, pentagonal, square, or triangular polygonal ridges (see also Fig. 2d). It is likely that the pentagonal shape appears due to the presence of the five-handed bead that is first attaching to the substrate in our simulation. The influence of isolated beads of fivefold symmetry on a sphere [69, 70] will be discussed separately in Section 6.

4.2 Asphericity

Next we characterize the shape of the deformed shells more quantitatively. For this purpose, we first calculate the moment of inertia tensor defined by [71, 72]

$$I_{\alpha\beta} = \frac{1}{2N^2} \sum_i \sum_j (r_{i,\alpha} - r_{j,\alpha})(r_{i,\beta} - r_{j,\beta}), \quad (34)$$

where \mathbf{r}_i is the position of bead i , and $\alpha, \beta = x, y, z$. The sum is taken over bead positions in a given configuration. The three eigenvalues of $I_{\alpha\beta}$ are ordered according

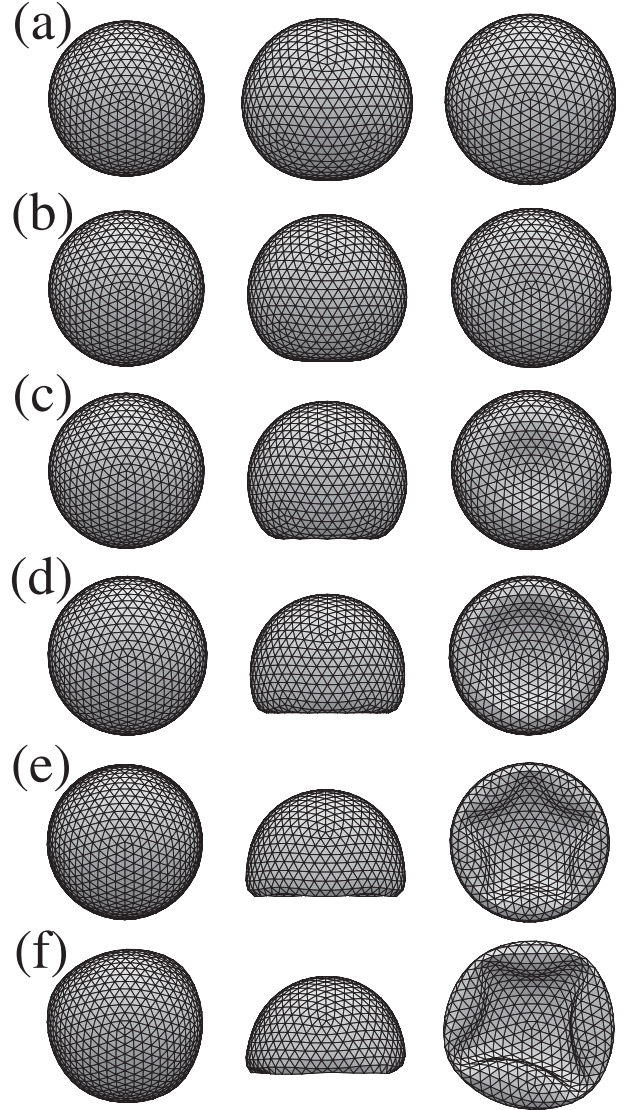


Fig. 3. Top, side and bottom views of the equilibrated configurations of adhering spherical shells when the sets of the scaled elastic constants ($C_s/\epsilon, C_b/\epsilon$) are (a) (100, 50), (b) (100, 10), (c) (100, 5), (d) (100, 2), (e) (100, 1.2), (f) (100, 1.1).

to magnitude $\lambda_1 \leq \lambda_2 \leq \lambda_3$. The directions of the principal axes are given by the eigenvectors corresponding to these eigenvalues.

As a quantitative measure of the asphericity of the deformed shell, we have calculated the following three quantities [68]:

$$\Gamma_1 = \frac{\lambda_1}{\lambda_3}, \quad (35)$$

$$\Delta = \frac{\lambda_1^2 + \lambda_2^2 + \lambda_3^2 - (\lambda_1\lambda_2 + \lambda_2\lambda_3 + \lambda_3\lambda_1)}{(\lambda_1 + \lambda_2 + \lambda_3)^2}, \quad (36)$$

and

$$S = \frac{(\lambda_1 - \bar{\lambda})(\lambda_2 - \bar{\lambda})(\lambda_3 - \bar{\lambda})}{2\lambda^3}, \quad (37)$$

where $\bar{\lambda} = (\lambda_1 + \lambda_2 + \lambda_3)/3$ in S . The range of each value is $0 \leq \Gamma_1 \leq 1$, $0 \leq \Delta \leq 1$, or $-\frac{1}{8} \leq S \leq 1$. The value of Γ_1 is

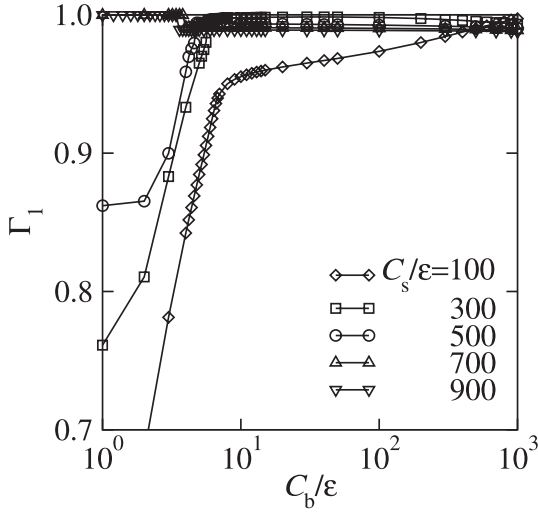


Fig. 4. The anisotropic factor Γ_1 defined in equation (35) as a function of the scaled bending constant C_b/ϵ for $C_s/\epsilon = 100, 300, 500, 700,$ and 900 .

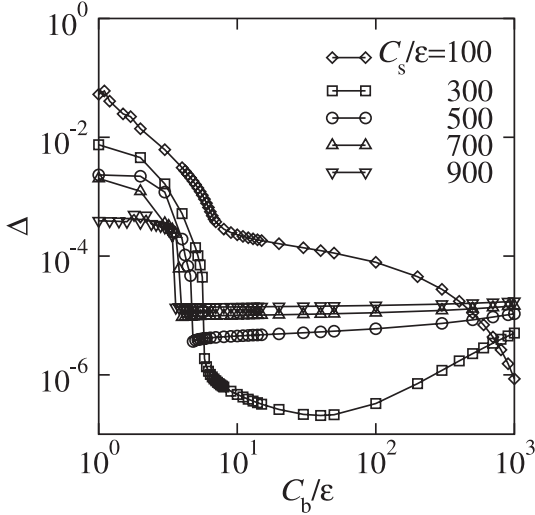


Fig. 5. The anisotropic factor Δ defined in equation (36) as a function of the scaled bending constant C_b/ϵ for $C_s/\epsilon = 100, 300, 500, 700,$ and 900 .

unity when the shell is completely isotropic. Conversely, Δ vanishes when the shell is isotropic, while it deviates from zero for an anisotropic configuration. Negative S means that the shell is oblate, while it is positive when the shell is prolate. In Figures 4–6, we have respectively plotted Γ_1 , Δ , and $|S|$ as a function of C_b/ϵ for various different values of C_s/ϵ ranging from 100 to 900.

We begin by discussing Figure 4. For $C_s/\epsilon = 100$, Γ_1 decreases monotonically as C_b/ϵ becomes smaller. In this case, the buckling occurs at around $C_b/\epsilon \approx 10$ when the slope of the curve changes drastically. A similar buckling behavior is observed both for $C_s/\epsilon = 300$ and 500 . Unless the shell is buckled strongly as in the anisotropic buckling region, the largest and the second largest eigenvalues are almost equal; $\lambda_2 \approx \lambda_3$. This means that the deformation is isotropic in the xy -direction (see Figs. 3a to d).

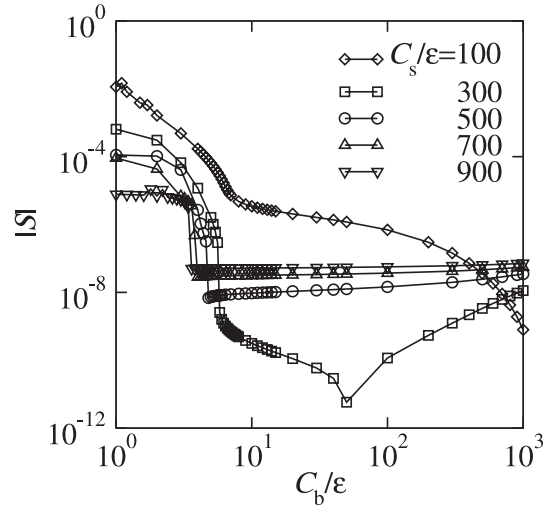


Fig. 6. The absolute value of the anisotropic factor $|S|$ defined in equation (37) as a function of the scaled bending constant C_b/ϵ for $C_s/\epsilon = 100, 300, 500, 700,$ and 900 .

In Figure 5, the buckling of the shell is manifested in the sharp increase of Δ as C_b/ϵ is decreased. There are jumps of Δ for larger values of C_s/ϵ , which indicates the occurrence of a *discontinuous* buckling transition. For $C_s/\epsilon = 100$, on the other hand, Δ changes continuously and a *continuous* buckling takes place. It is worthwhile to mention that Δ attains its minimum at C_b/ϵ larger than its threshold value of the buckling. For $C_s/\epsilon = 300$, the minimum and the discontinuous jump of Δ occur at different C_s/ϵ , whereas they coincide with each other for larger C_s/ϵ . In the continuum limit, Δ should vanish for a perfect spherical shell. However, due to our finite discretization of the shell, a small asphericity exists even in the initial undeformed configuration, *i.e.*, $\Delta \approx 3.1 \times 10^{-5}$ for $N = 812$. Since this value is slightly larger than the minimum values of Δ , the appearance of minima in Figure 5 can partially be an artifact of the discretization. Although the origin of the minima in Δ is not completely clear, we note that it has nothing to do with the global deformation of the shell.

The measured value of S is always negative, and in Figure 6, we have plotted the absolute value of S as a function of C_b/ϵ . Negative S reflects the oblate pancake-like shape of the deformed shells. We see here that the behaviors of Δ (Fig. 5) and $|S|$ (Fig. 6) are quite analogous. From Figures 5 and 6, we conclude that the buckling can occur both in continuous and discontinuous manners.

4.3 Minimized energy

Here we look at the minimized energy of the deformed shell. Figure 7 shows all the energies equations (28–30) and the total energy E_{tot} as a function of C_b/ϵ when $C_s/\epsilon = 900$. In this case, the shell exhibits a discontinuous buckling transition at around $(C_b/\epsilon)^* \approx 3.5$ as indicated by the dashed line. When the value of C_b/ϵ crosses this critical value from above, both the stretching energy E_s and the bending energy E_b increases abruptly. These

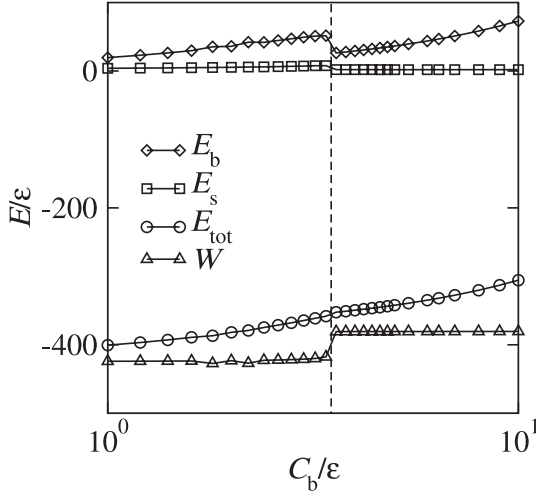


Fig. 7. The minimized total energy E_{tot}/ϵ as a function of C_b/ϵ for $C_s/\epsilon = 900$. The three energies E_s , E_b , and W contributing to E_{tot} are also shown. The discontinuous buckling transition occurs at $(C_b/\epsilon)^* \approx 3.5$ indicated by the dashed line.

losses in the elastic energies are compensated by the gain in the van der Waals energy W which decreases discontinuously at the transition point. In other words, the shell buckles at the expense of the elastic energy when the adhesive force is strong enough. Interestingly, however, the discontinuity in E_{tot} around the transition point is very small.

For different values of C_s/ϵ , the behaviors of each energy are qualitatively similar when the discontinuous buckling occurs. However, the discontinuities in E_b and W at the transition are smaller when C_s/ϵ becomes smaller. To see this more clearly, we have plotted in Figure 8 the bending energy E_b/ϵ as a function of C_b/ϵ for various C_s/ϵ as before. When the discontinuous buckling occurs for $C_s/\epsilon \geq 300$, all the data fall onto a single curve in the large C_b/ϵ region. Moreover, E_b/ϵ is almost proportional to C_b/ϵ because the shell deforms only slightly (small deformation regime). By contrast, the continuous buckling takes place when $C_s/\epsilon = 100$ for which the data deviate from others.

Figure 9 is a similar plot of the adhesion energy W/ϵ as a function of C_b/ϵ . When C_s/ϵ is larger than 300, W/ϵ is almost independent of C_b/ϵ in the unbuckled region, but starts to decrease as the buckling takes place. For $C_s/\epsilon = 100$, however, W/ϵ decreases continuously as C_b/ϵ is reduced.

4.4 Indentation length

To investigate the nature of the buckling transition in more detail, we have measured the indentation lengths H_1 and H_2 as defined in Figure 10. In Figure 11, we plot H_1/R as a function of C_b/ϵ for various C_s/ϵ ranging from 100 to 900. Here the radius of the undeformed spherical shell is $R = 0.75\sigma$ when $N = 812$ (see Sect. 4.6 or Tab. 1). In accordance with the aforementioned discussion, H_1 changes discontinuously at the transition point

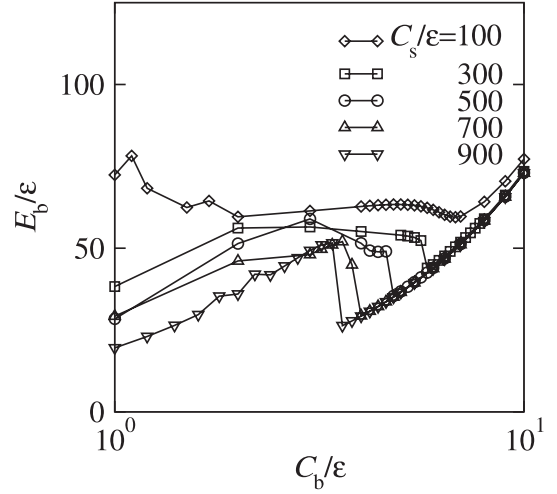


Fig. 8. The scaled bending energy E_b/ϵ as a function of the scaled bending constant C_b/ϵ for $C_s/\epsilon = 100, 300, 500, 700$, and 900.

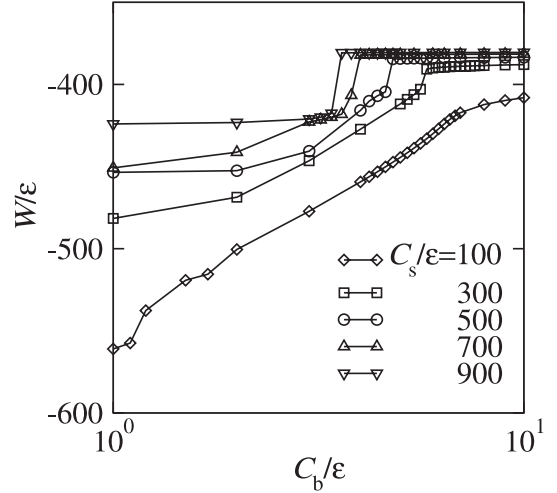


Fig. 9. The scaled adhering energy W/ϵ as a function of the scaled bending constant C_b/ϵ for $C_s/\epsilon = 100, 300, 500, 700$, and 900.

for larger C_s/ϵ , revealing the first-order nature of the buckling transition. This discontinuous buckling transition takes place between the disk formation regime and the isotropic buckling regime (Figs. 2b and c). Hence the contact region changes from a disk to a ring at the transition point.

In the same way, we plot H_2/R as a function of C_b/ϵ in Figure 12. The length H_2 deviates from zero only if the shell buckles for which the behaviors of H_1 and H_2 are almost identical to each other. This result indicates that the geometry of the buckled region is represented by a mirror image of the original undeformed shell.

Figure 13 shows the variation of the total indentation length H defined by

$$H = H_1 + H_2. \quad (38)$$

The discontinuous jump in H/R becomes smaller as C_s/ϵ is decreased, and finally vanishes at around $C_b/\epsilon \approx 6.1$

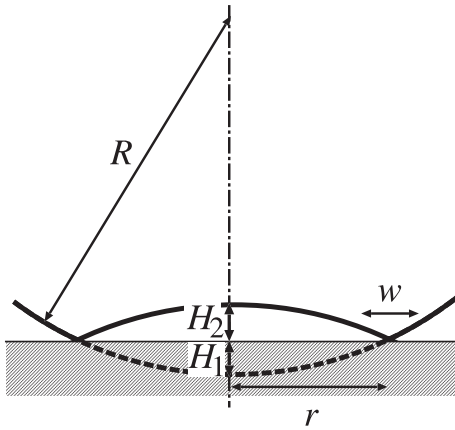


Fig. 10. Notation of the indentation lengths H_1 and H_2 in the isotropic buckling regime. The total indentation length is given by $H = H_1 + H_2$. R is the radius of the undeformed spherical shell. r is the radius of the circular bending strip whose width is denoted by w .

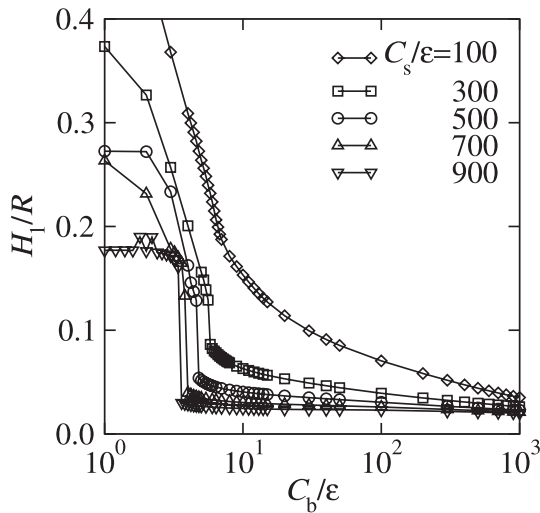


Fig. 11. The scaled indentation length H_1/R as a function of the scaled bending constant C_b/ϵ for $C_s/\epsilon = 100, 300, 500, 700,$ and 900 .

(the filled circle). The corresponding critical indentation length is $H_1/R \approx 0.18$, and that of the stretching constant is $C_s/\epsilon \approx 210$. Below this value of C_s/ϵ , the buckling occurs continuously rather than discontinuously.

We immediately note that Figure 13 is very reminiscent of the isotherms of non-ideal gases in the pressure-volume plane. Analogous to the liquid-gas coexistence region of van der Waals fluids, the region of discontinuous transition has been shaded in Figure 13. In the present model, the parameter C_s/ϵ plays a role similar to the temperature of van der Waals fluids. Another similar phenomenon is the volume transition of gels which is induced either by changing the temperature or the ionic strength.

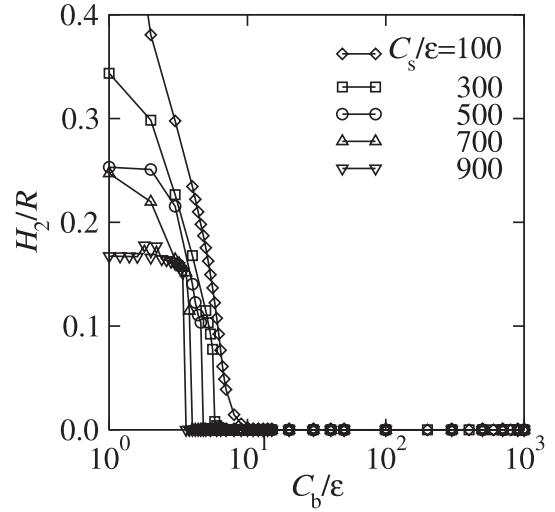


Fig. 12. The scaled indentation length H_2/R as a function of the scaled bending constant C_b/ϵ for $C_s/\epsilon = 100, 300, 500, 700,$ and 900 .

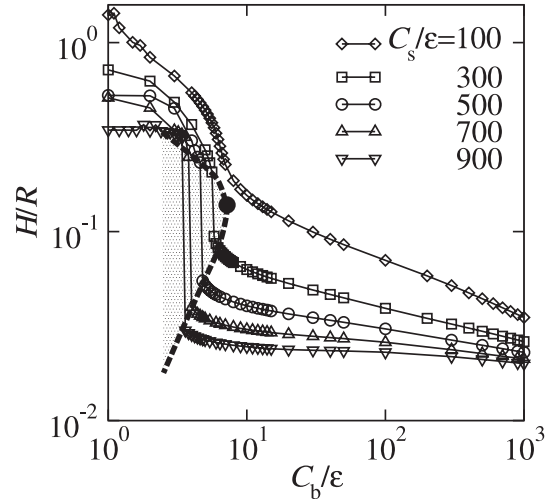


Fig. 13. The total indentation length H/R as a function of the scaled bending constant C_b/ϵ for $C_s/\epsilon = 100, 300, 500, 700,$ and 900 . The filled circle being located roughly at $(C_b/\epsilon, H/R, C_s/\epsilon) = (6.1, 0.18, 210)$ indicates the point at which the discontinuity vanishes.

4.5 Scaling relation

Here we analyze the geometry of the buckled shell from a different aspect. In Figure 14, we have plotted the relation between the scaled ring radius r/R and the total indentation length H/R (see Fig. 10 and Eq. (38)) for various combinations of C_b/ϵ and C_s/ϵ when $N = 812$. Different points represented by the same symbol correspond to different C_b/ϵ values having the same C_s/ϵ values. Interestingly, most of the data collapse onto a single line, and we find that a scaling relation $r/R \sim (H/R)^{1/2}$ holds in this regime. This scaling relation results from a simple geometrical consideration. As we will discuss in the next section, the buckled region is almost a mirror image of the original undeformed shell.

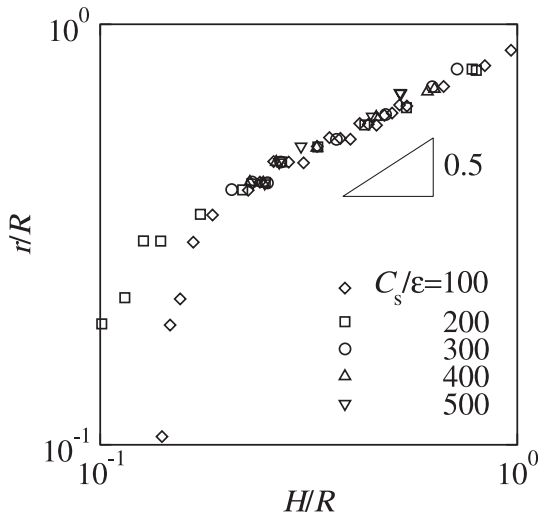


Fig. 14. Relation between the scaled ring radius r/R defined in Figure 10 and the scaled total indentation H/R for various combinations of C_s/ϵ (ranging from 100 to 500) and C_b/ϵ . Most of the data collapse onto a single line which gives the scaling relation $r/R \sim (H/R)^{0.5}$.

The data deviate from a straight line when H/R is small because the deformation of the shell cannot be described by the geometry in Figure 10. Moreover, the above scaling relation does not hold in the anisotropic buckling regime in which the polygonal ridges are formed (see Figs. 3e or f).

4.6 Size dependence

So far, we have discussed only the results when $N = 812$. Even the shell size N is varied, the qualitative properties of the deformation are unchanged from the case of $N = 812$. For example, the total indentation length H behaves similarly to Figure 13 although the location of the critical point shifts systematically. Table 1 summarizes the values of the critical point for four different sizes $N = 92, 272, 812$ and 2432 . We have simultaneously listed the values of L_0/σ , R/σ , and R/L_0 for each size.

Roughly speaking, the critical values of the elastic constants $(C_s/\epsilon)_c$ and $(C_b/\epsilon)_c$ are larger for larger shells. On the other hand, the values of $(H/R)_c$ decreases for larger shells. This tendency holds true as long as the potential range satisfies $R/\sigma \leq 1$. When R/σ is much larger than unity, the buckling does not occur. It is reasonable to think that larger shells with a small curvature can be easily deformed due to the reduced coupling effect.

4.7 Hysteresis

If the initial shape of the shell is far from a sphere, we sometimes could not find the global minimum within the conjugate gradient method. For complete spherical shells, on other hand, we could always obtain reasonable equilibrium configurations as depicted before. For the initial

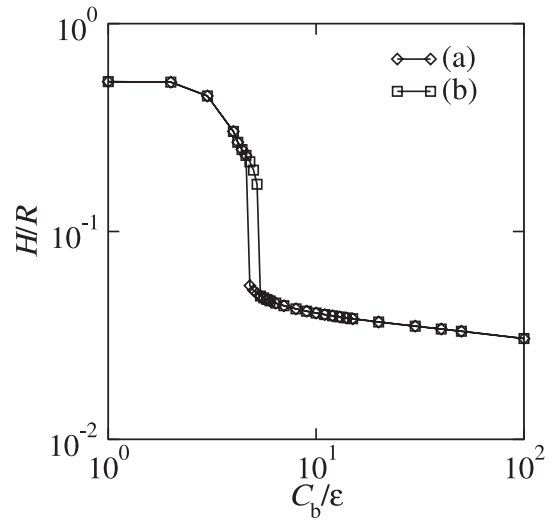


Fig. 15. The total indentation length H/R as a function of the scaled bending constant C_b/ϵ for two different initial configurations. The case (a) is the result when a spherical shell is used as the initial configuration. In the case of (b), the strongly buckled final configuration obtained when $C_s/\epsilon = 500$ and $C_b/\epsilon = 1$ is used as the initial configuration. There is a small hysteresis.

spherical configuration, the stretching energy E_s is relaxed in the absence of adhesion although the bending energy E_b is inherent. We remind that the effect of spontaneous curvature is not included in our model.

For certain parameter choices, however, the numerical results seem to depend on the initial configuration. In Figure 15, we have plotted the equilibrium total indentation length H/R obtained from the two different initial configurations but having the same elastic parameters. The case (a) is the result when a spherical shell is used as the initial configuration. In the case of (b), the strongly buckled final configuration obtained when $C_s/\epsilon = 500$ and $C_b/\epsilon = 1$ is used as the initial configuration. Although most of the results obtained from these two cases coincide with each other, there is a slight difference in buckling transition point, which results in a small hysteresis. The observed hysteresis becomes more remarkable for smaller C_s/ϵ and/or C_b/ϵ , but we did not investigate it systematically since it is impossible to scan all the allowed initial configurations.

4.8 Multi-buckling

Finally, we show a peculiar type of adhesion-induced deformation which cannot be classified into the four regimes as described in Section 4.1. Figure 16 shows the equilibrium configuration when the parameters are $(C_s/\epsilon, C_b/\epsilon) = (30, 1)$ corresponding to a relatively strong adhesion regime. Interestingly, the buckling transition occurs twice in this case, *i.e.*, a new buckling takes place inside the original buckled region. We call this phenomenon as the *multi-buckling transition* which is observed when



Fig. 16. Top, side and bottom views of the equilibrated configurations of an adhering spherical shell when the sets of the scaled elastic constants are $(C_s/\epsilon, C_b/\epsilon) = (30, 1)$.

the adhesion is strong enough to induce the second buckling. For much larger shells, one would expect to see the multi-buckling which exhibits more than triple bucklings. Although we are not aware of such a unique shape in the real life, it would be very interesting to find the multi-buckled state experimentally. Biological cells adhering onto a rigid substrate may be one of the possible systems to observe the multi-buckling because the binding energy between the cell membranes and substrate can be fairly large. We comment here that a cascade of buckling was observed by compressing thin plates [73].

5 Scaling theory

Based on the continuum shell theory, as described in Section 2, we now interpret the deformation of the shell within the scaling argument [18]. Attention will be paid to the cases in Figures 2b and c, *i.e.*, the disk formation regime (case I) and the isotropic buckling regime (case II).

First, we discuss how the parameters in the discretized model are related to those in the continuum theory such as the Young's modulus or the Poisson's ratio. We remind again that both C_s and C_b in the discretized model have the dimension of energy. Then according to equation (25), we can relate them as

$$\frac{C_s}{L_0^2} \sim \frac{Yh}{1-\nu^2}, \quad (39)$$

$$C_b \sim \frac{Yh^3}{1-\nu^2}, \quad (40)$$

except the prefactors. Note that the three-dimensional Young's modulus Y has the dimension of energy per volume, and the Poisson's ratio is dimensionless. From the above relations, the effective thickness h and the Young's modulus are given by

$$h \sim (C_b L_0^2 / C_s)^{1/2}, \quad (41)$$

$$Y \sim C_s^{3/2} / C_b^{1/2} L_0^3. \quad (42)$$

In order to determine the numerical factors, the geometry of the network should be specified. For a two-dimensional triangular lattice, Seung and Nelson showed that the following relations holds [63, 74]:

$$\frac{C_s}{L_0^2} = \frac{\sqrt{3}}{2} Yh, \quad (43)$$

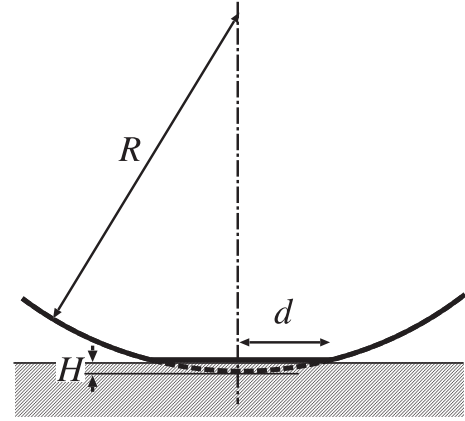


Fig. 17. Notation of the indentation lengths H in the disk formation regime. R is the radius of the undeformed spherical shell. d is the radius of the circular disk.

$$\nu = \frac{1}{3}, \quad (44)$$

$$C_b = \frac{\sqrt{3}}{16} Yh^3. \quad (45)$$

Combining these three relations, h and Y are given by

$$h = (8C_b L_0^2 / C_s)^{1/2}, \quad (46)$$

$$Y = \frac{1}{\sqrt{6}} \frac{C_s^{3/2}}{C_b^{1/2} L_0^3}. \quad (47)$$

In the disk formation regime (case I), the effect of adhesion is weak so that the shell deforms only slightly at the bottom as we have seen in Figure 2b. This situation is analogous to the case of a shell subjected to a small localized force [18]. Let d be the dimension of the deformed region which is caused by the contact between the shell and the substrate as depicted in Figure 17. The out-of-plane displacement ζ (see Eq. (11)) in the deformed region can be identified as the indentation length H , *i.e.*, $\zeta \sim H$. Following the continuum treatment, the strain tensor is of the order of $\zeta/R \sim H/R$. Hence the total stretching energy is

$$E_s \sim YhH^2 d^2 / R^2, \quad (48)$$

where we have multiplied the area of the deformed region d^2 . The fact that ζ varies considerably over a distance d gives the curvature $\zeta/d^2 \sim H/d^2$. Then the total bending energy behaves as

$$E_b \sim Yh^3 H^2 / d^2. \quad (49)$$

Note that the stretching energy increases and bending energy decreases with increasing d .

The size d is provided by the condition that these two energies balance:

$$d \sim (hR)^{1/2} \sim (C_b L_0^2 / C_s)^{1/4} R^{1/2}, \quad (50)$$

where we have used equation (41). Hence the area of the contact region $S^{(1)}$ for the case I scales as

$$S^{(1)} \sim d^2 \sim hR \sim (C_b L_0^2 / C_s)^{1/2} R. \quad (51)$$

The minimized total elastic energy $E_e = E_s + E_b$ scales as

$$\begin{aligned} E_e^{(I)} &\sim Yh^2H^2/R \\ &\sim (C_bC_s/L_0^2)^{1/2}H^2/R. \end{aligned} \quad (52)$$

Varying this with respect to H gives the force:

$$f^{(I)} \sim (C_bC_s/L_0^2)^{1/2}H/R, \quad (53)$$

which is proportional to H . This result indicates the linear Hooke's law of the deformation.

In the isotropic buckling regime (case II), on the other hand, the adhesion is strong enough for the shell to undergo the buckling as in Figure 2c. Then most of the elastic energy is concentrated over a narrow bending strip of width w and radius r as defined in Figure 10. The buckled region is assumed to be a spherical cap which is a mirror image of its original shape. We remind that the assumption of vanishing spontaneous curvature plays an important role here. Then the following relation holds according to the simple geometrical reason [18]:

$$r \sim H^{1/2}R^{1/2}, \quad (54)$$

where H is the total indentation length. This explains the scaling relation which we found in our simulation (see Fig. 14).

Since the order of magnitude of the displacement of a point within the bending strip is $\zeta \sim wr/R$, the strain is given by $\zeta/R \sim wr/R^2$, and the curvature is $\zeta/w^2 \sim r/Rw$. Then the stretching energy and bending energy scale as

$$E_s \sim Yh(wr/R^2)^2wr \sim Yhw^3r^3/R^4, \quad (55)$$

and

$$E_b \sim Yh^3(r/Rw)^2wr \sim Yh^3r^3/R^2w, \quad (56)$$

respectively. Here wr is the area of the bending strip. Minimizing these two energies with respect to w , we obtain

$$w \sim (hR)^{1/2} \sim (C_bL_0^2/C_s)^{1/4}R^{1/2}. \quad (57)$$

Note that the scaling of d in equation (50) and that of w are the same. From equations (54) and (57), the area of the bending strip that contacts with the substrate as in Figure 2c is given by

$$S^{(II)} \sim wr \sim (C_bL_0^2/C_s)^{1/4}H^{1/2}R. \quad (58)$$

The minimized total elastic energy is given by

$$\begin{aligned} E_e^{(II)} &\sim Yh^{5/2}r^3/R^{5/2} \\ &\sim Yh^{5/2}H^{3/2}/R \\ &\sim C_b^{3/4}(C_s/L_0^2)^{1/4}H^{3/2}/R. \end{aligned} \quad (59)$$

In this case, the required force f is

$$f^{(II)} \sim C_b^{3/4}(C_s/L_0^2)^{1/4}H^{1/2}/R. \quad (60)$$

In contrast to equation (53), this relation is non-linear.

So far the discussion is valid as long as H is fixed and given. We now consider how the indentation length H can be related to the strength of adhesion. Let v be the van der Waals energy per unit area. It was shown in reference [51] that v can be approximately given by $v \sim A/(12\pi\delta^2)$, where A is the Hamaker constant and δ is an atomic cutoff. Then the total adhesion energy is estimated by

$$E_a \sim vS, \quad (61)$$

where S is the contact area. In the disk formation regime (case I), we use equation (51) for the contact area. If the deformations are driven by van der Waals adhesion, the adhesion energy E_a is expected to balance with the elastic energy E_e given by equation (52). By setting $E_a \sim E_e^{(I)}$, we arrive at the estimate for the indentation length H :

$$H^{(I)} \sim v^{1/2}(L_0^2/C_s)^{1/2}R, \quad (62)$$

for given v and R . In the isotropic buckling regime (case II), we use equation (58) for the contact area. By setting $E_a \sim E_e^{(II)}$, we get

$$H^{(II)} \sim vC_b^{-1/2}(L_0^2/C_s)^{1/2}R^2, \quad (63)$$

which is a different scaling.

Comparing equations (51) and (58), we see that the contact area of the bending strip becomes larger than that of the disk ($S^{(I)} < S^{(II)}$) when the relation $H > (C_bL_0^2/C_s)^{1/2}$ holds. Since the right hand side of this inequality scales similarly with the effective thickness h (see Eqs. (41) or (46)), we see that the transition from the disk formation regime to the isotropic buckling regime occurs typically for a deformation $H \geq h$. The increase in the contact area between the shell and the substrate results in the gain in the van der Waals adhesion energy, and hence W decreases when the buckling takes place as seen in Figure 9.

Let us check if this scaling argument holds true in our numerical simulation. As a rough estimate of the transition point, we pay attention to the critical point in Figure 13 which separates the discontinuous and continuous buckling behaviors. We mentioned in the previous section that the critical point appears when the combination of the elastic constants are $(C_b/\epsilon)_c \approx 6.1$ and $(C_s/\epsilon)_c \approx 210$ for $N = 812$ (see also Tab. 1). By using equation (46), we can deduce the effective thickness to be $(h/R)_c \approx 0.064$. On the other hand, the numerically obtained critical indentation length is $(H/R)_c \approx 0.18$. By taking the ratio between H and h , we obtain the relation $H \approx 2.8h$ at the critical point. This result indeed confirms the fact that the buckling transition takes place when the indentation length exceeds the shell thickness.

We have performed the similar analysis for other shells which have different sizes N . The results are summarized again in Table 1. The ratio H/h (the last column) is roughly 2–3 with the largest uncertainty for $N = 92$. Remarkably enough, this value is almost independent of N , although the location of the critical point differs significantly between the different sizes. It is very interesting

to see that the universal property of the shell manifests itself at the critical point of the buckling transition. As we shall discuss in the next section, the general condition for buckling transitions seems to hold in various systems ranging from nanoscale to macroscale.

6 Discussion

In order to bridge between our results and real materials, we first give some typical numbers to the model parameters. In the case of a layered material made of carbon, the two-dimensional Young's modulus and the bending rigidity are roughly 1.3×10^5 erg/cm² and 1.6×10^{-12} erg, respectively [75]. Assuming that the adhesion energy ϵ is the order of thermal energy $k_B T$, we can deduce the model parameters as $C_s/\epsilon \approx 480$ and $C_b/\epsilon \approx 40$. According to Figure 13, the adhesion of a single-walled fullerene (with radius $R/\sigma \approx 0.75$) should correspond to a point well above the critical point. In this regime, the fullerene may deform as in Figure 2b, which is consistent with the previous prediction [51].

Other example of a spherical shell is a polyelectrolyte multilayer capsule [42–45]. Such a material is produced using layer-by-layer coating of dissolvable colloids and subsequent dissolution of the core material. These capsules offer the advantage that they can be prepared with well-controlled radius and shell thickness. The three-dimensional Young's modulus of the capsule was measured to be 500–750 MPa [42, 43] or 1.5–2 GPa [44, 45], but its thickness h tends to be in the 10 nm range. Since this gives fairly large bending rigidity of the order of $C_b/\epsilon \approx 10^4$, van der Waals adhesion only would not cause a considerable deformation of a microcapsule and belong to the small deformation regime as in Figure 2a.

However, it was shown in reference [45] that other attractive interaction such as electrostatic interaction leads to a strong adhesion of microcapsules. In fact, anionic microcapsules on cationic glass resulted in a truncated sphere topology with a circular adhesion disk. This situation obviously corresponds to the disk formation regime in our simulation. The dependence of the adhesion disk on the shell thickness is found to be in agreement with the previous theoretical prediction [18, 51]. Furthermore, microcapsules become unstable and buckle due to the osmotic pressure difference between inside and outside the shell [42, 43]. The critical osmotic pressure depends on the capsule radius and the shell thickness.

As briefly mentioned in Introduction, there are several controlled mechanical experiments which deal with the buckling of spherical shells. For example, Dubreuil *et al.* compressed the above mentioned polyelectrolyte microcapsules using AFM [44]. The shape of the deformed shell was monitored by reflection interference contrast microscopy. They measured the relation between force and deformation, and revealed that the capsule first deforms only weakly. As the deformation becomes larger, an increase in the contact area is observed, which is followed by the buckling transition. In a more recent investigation on the same system, both the isotropic buckling and

anisotropic buckling are distinguished [76]. Although a high hysteresis between the loading and unloading curve was detected, the capsule stayed elastic. The observed sequence of deformation caused by the compression is very similar to what we see in our simulation.

Pauchard and Rica studied the deformation of a ping-pong ball which is forced to be in contact with a rigid plate [37, 38]. In their work, the boundary of the half-sphere was fixed in order to avoid non-axisymmetric deformations. For low applied forces, the shell flattens against the horizontal plate. For higher compression forces, a discontinuous buckling transition occurs when the deformation is close to twice the thickness of the shell; $H/h \approx 2.4$. This value cannot be directly compared with the corresponding ratio at the critical point in our simulation ($H/h \approx 2.8$) since the buckling is discontinuous for a ping-pong ball. However the fact that the deformation becomes larger than the shell thickness is the required condition even for the buckling of a ping-pong ball. Moreover, the sequence of the deformation is in good agreement with our simulation results, although their experimental set-up is not identical to our model of adhesion. Interestingly, the polygonal structures associated with the anisotropic buckling as in Figure 2d were also formed when a localized point force was applied to the shell [37, 38].

In a smaller scale experiment, the microrheology of self-assembled actin-coated vesicles was studied using optical tweezers and single-particle tracking [35]. The actin filaments mimic cytoskeletal networks in cells, and they increase the bending modulus of the membrane up to around $100 k_B T$. A buckling instability was observed when a large localized force of the order of 0.5 pN is applied perpendicular to this vesicle [36]. This deformation involves both the stretching and bending contributions, and has been interpreted in terms of the shell theory as in the present paper. The thickness of the actin-coated vesicle is roughly $h \approx 100$ nm, and it buckles when the deformation exceeds $H \approx 200$ nm. Hence the ratio between the two lengths is $H/h \approx 2$ at the threshold of the buckling. We therefore see that the condition $H > h$ determines the onset of various types of buckling transitions in different length scales.

As a result of the Delaunay triangulation of the spherical surface, there are always 12 grid points which have five neighbors as explained in Section 3. Recently, the faceting of spherical shells associated with 12 isolated points of fivefold symmetry was argued by Lidmar *et al.* [70]. They introduced the so called Föppl-von Kármán number of a spherical shell defined by

$$\tau = \frac{\hat{Y} R^2}{\kappa}, \quad (64)$$

where \hat{Y} is the two-dimensional Young's modulus [74]. From the relation $\hat{Y} = Yh$ and equation (26), we note that τ is proportional to the square of the ratio between the radius R and thickness h of the shell; $\tau \sim (R/h)^2$. It is reported in reference [70] that, in the absence of adhesion, a significant deviation from a perfect spherical shape takes place when τ becomes of the order of 10^3 . This instability

results in the faceting of the shell, which is manifested in sufficiently large viruses composed of protein capsomers.

As a rough comparison with this prediction, we estimate the Föpplé-von Kármán number τ at the critical point for each size N . Using the numbers of $(h/R)_c$ listed in Table 1, we can estimate τ to be less than 10^3 for $N = 92, 272, 812$, but becomes roughly 10^3 for $N = 2432$. Hence the faceting of the shell may be irrelevant for most of the cases as long as the buckling is concerned. One difference between our model and that used in reference [70] is that not all the springs have the equal natural length in the present case. More precisely, the springs which are connected to the five-handed beads have slightly smaller natural length than those connected to the six-handed beads. Hence the spherical shape is more stable in our numerical simulation and the defect-induced buckling is suppressed. However, it is possible that the anisotropic buckling is triggered by the singular disclinations as mentioned in Section 4. This can be important when the buckled region creates a polygonal structure.

In a recent experiment by Pauchard and Couder, the buckling of shell-shaped membranes was observed using droplets of suspension [40]. As evaporation goes on, a spherical droplet on a super-hydrophobic substrate first flattens at the top. Then the buckling starts at the top of the droplet, and the inverted region grows into an invagination. Although this behavior is dynamic in its nature, the sequence of deformation is similar to what we have described in the present paper. In the last stage, a transition to a toroidal shape was observed, which is interesting in the context of gastrulation of embryos. This phenomena is attributed to the inhomogeneity of the shell, *i.e.*, the elastic constants of the flattened part is smaller than the rest of the shell. The inhomogeneity in the elastic constants can play an important role such as in the domain formation in lipid bilayers [77]. Generalization to take into account the inhomogeneous elastic constants is straightforward, and will be examined in the future.

For red blood cells, it is reported that a strong adhesion produces a finite membrane tension [78, 79]. Such a spreading-induced tension can cause the rupture of cells. We have not included the effect of tension in our simulation, but can make the following argument. Since the presence of a positive tension tends to shrink the total area of the shell, we expect that it will effectively reduce the natural length of each spring. Since this results in a smaller shell thickness (see Eq. (41)), it is possible that a shell with a tension can buckle easier than a tensionless shell. In reality, buckling may induce rupture since the elastic energies will be localized in a small region.

As a final remark, we note that the notion of spontaneous curvature of shells is different from that of fluid membranes. For elastic shells, one needs to introduce defects to produce a preferred curvature, which depends on how the shell is prepared. Hence the spontaneous curvature of shells is induced by a kinetic effect. For fluid membranes, on the other hand, spontaneous curvature is indeed a material constant.

7 Conclusion

We have investigated the deformation of the elastic shell adhering onto the substrate both numerically and theoretically. The sum of the stretching, bending, and adhesion energies is minimized using the conjugate gradient method. The deformation of the shell is characterized by the dimensionless parameters C_s/ϵ and C_b/ϵ . There are four different regimes of deformation: (i) small deformation regime, (ii) disk formation regime, (iii) isotropic buckling regime, and (iv) anisotropic buckling regime. As for the buckling transition, there are both discontinuous and continuous cases for large and small C_s/ϵ , respectively. These different cases are separated by the critical point. According to the scaling arguments, the buckling transition takes place when the indentation length exceeds the effective shell thickness, which is in good agreement with our numerical results. Moreover, the ratio between the indentation length and its thickness close to the critical point is roughly 2 even for different shell sizes. This general condition seems to hold in various experimental systems ranging from nanoscale to macroscale.

We thank A. Fery, R. Lipowsky, and S.A. Safran for useful discussions. This work is supported by the Ministry of Education, Culture, Sports, Science and Technology, Japan (Grant-in-Aid for Scientific Research No. 15540395).

References

1. T. Hwa, E. Kokufuta, T. Tanaka, Phys. Rev. A **44**, R2867 (1991)
2. X. Wen, C. Garland, T. Hwa, M. Kardar, E. Kokufuta, Y. Li, M. Orkisz, T. Tanaka, Nature **355**, 426 (1992)
3. M.S. Spector, E. Naranjo, S. Chiruvolu, J.A. Zasadzinski, Phys. Rev. Lett. **73**, 2867 (1994)
4. L. Bourdieu, J. Daillant, D. Chatenay, A. Braslau, D. Colson, Phys. Rev. Lett. **72**, 1502 (1994)
5. A. Saint-Jalmes, F. Graner, F. Gallet, B. Houchmandzadeh, Europhys. Lett. **28**, 565 (1994)
6. A. Saint-Jalmes, F. Gallet, Eur. Phys. J. B **2**, 489 (1998)
7. C.F. Schmidt, K. Svoboda, N. Lei, I.B. Petsche, L.E. Berman, C.R. Safinya, G.S. Grest, Science **259**, 952 (1993)
8. A.A. Boulbitch, Phys. Rev. E **57**, 2123 (1998)
9. E.M. Kramer, T.A. Witten, Phys. Rev. Lett. **78**, 1303 (1997)
10. B.A. DiDonna, T.A. Witten, S.C. Venkataramani, E.M. Kramer, Phys. Rev. E **65**, 016603 (2001)
11. T.A. Witten, H. Li, Europhys. Lett. **23**, 51 (1993)
12. A.E. Lobkovsky, S. Gentges, H. Li, D. Morse, T.A. Witten, Science **270**, 1482 (1995)
13. A.E. Lobkovsky, Phys. Rev. E **53**, 3750 (1996)
14. A.E. Lobkovsky, T.A. Witten, Phys. Rev. E **55**, 1577 (1997)
15. B.A. DiDonna, T.A. Witten, Phys. Rev. Lett. **87**, 206105 (2001)
16. B.A. DiDonna, Phys. Rev. E **66**, 016601 (2002)
17. K. Matan, R.B. Williams, T.A. Witten, S.R. Nagel, Phys. Rev. Lett. **88**, 076101 (2002)

18. L.D. Landau, E. M. Lifshitz, *Theory of Elasticity* (Pergamon, Oxford, 1986)
19. M. Ben Amar, Y. Pomeau, Proc. R. Soc. Lond. A **453**, 729 (1997)
20. E. Cerda, L. Mahadevan, Phys. Rev. Lett. **80**, 2358 (1998)
21. S. Chaïeb, F. Melo, J.-C. Gémard, Phys. Rev. Lett. **80**, 2354 (1998)
22. S. Chaïeb, F. Melo, Phys. Rev. E **60**, 6091 (1999)
23. E. Cerda, S. Chaïeb, F. Melo, L. Mahadevan, Nature **401**, 46 (1999)
24. B. Audoly, Phys. Rev. Lett. **83**, 4124 (1999)
25. B. Audoly, B. Roman, A. Pocheau, Eur. Phys. J. B **27**, 7 (2002)
26. B. Audoly, A. Boudaoud, Phys. Rev. Lett. **91**, 086105 (2003)
27. A. Boudaoud, P. Patrício, Y. Couder, M. Ben Amar, Nature **407**, 718 (2000)
28. T. Mora, A. Boudaoud, Europhys. Lett. **59**, 41 (2002)
29. E. Cerda, K. Ravi-Chandar, L. Mahadevan, Nature **419**, 579 (2002)
30. E. Cerda, L. Mahadevan, Phys. Rev. Lett. **90**, 074302 (2003)
31. S. Komura, R. Lipowsky, J. Phys. France II **2**, 1563 (1992)
32. Z. Zhang, H.T. Davis, D.M. Kroll, Phys. Rev. E **48**, R651 (1993)
33. S. Komura, in *Vesicles*, edited by M. Rosof (Marcel Dekker, 1996), pp. 198–236
34. H. Yoon, J.M. Deutch, Phys. Rev. E **56**, 3412 (1997)
35. E. Helfer, S. Harlepp, L. Bourdieu, J. Robert, F.C. MacKintosh, D. Chatenay, Phys. Rev. Lett. **85**, 457 (2000)
36. E. Helfer, S. Harlepp, L. Bourdieu, J. Robert, F.C. MacKintosh, D. Chatenay, Phys. Rev. Lett. **87**, 088103 (2001)
37. L. Pauchard, Y. Pomeau, S. Rica, C. R. Acad. Sci. Paris **324**, 411 (1997)
38. L. Pauchard, S. Rica, Phil. Mag. B **78**, 225 (1998)
39. L. Pauchard, C. Allain, Europhys. Lett. **62**, 897 (2003)
40. L. Pauchard, Y. Couder, Europhys. Lett. **66**, 667 (2004)
41. N. Tsapis, E.R. Dufresne, S.S. Sinha, C.S. Riera, J.W. Hutchinson, L. Mahadevan, D.A. Weitz, Phys. Rev. Lett. **94**, 018302 (2005)
42. C. Gao, S. Leporatti, S. Moya, E. Donath, H. Möhwald, Langmuir **17**, 3491 (2001)
43. C. Gao, E. Donath, S. Moya, V. Dudnik, H. Möhwald, Eur. Phys. J. E **5**, 21 (2001)
44. F. Dubreuil, N. Elsner, A. Fery, Eur. Phys. J. E **12**, 215 (2003)
45. N. Elsner, F. Dubreuil, A. Fery, Phys. Rev. E **69**, 031802 (2004)
46. O.I. Vinogradova, J. Phys.: Condens. Matter **16**, R1105 (2004) and references therein
47. T. Hertel, R. Martel, P. Avouris, J. Phys. Chem. B **102**, 910 (1998)
48. T. Hertel, R.E. Walkup, P. Avouris, Phys. Rev. B **58**, 13870 (1998)
49. M.-F. Yu, T. Kowalewski, R.S. Ruoff, Phys. Rev. Lett. **86**, 87 (2001)
50. S. Komura, K. Tamura, T. Kato, Eur. Phys. J. E **13**, 73 (2004)
51. U.S. Schwarz, S. Komura, S.A. Safran, Europhys. Lett. **50**, 762 (2000)
52. K. Miura, S. Kamiya, N. Sasaki, Phys. Rev. Lett. **90**, 055509 (2003)
53. K. Tamura, S. Komura, T. Kato, J. Phys.: Condens. Matter **16**, L421 (2004)
54. H. Hertz, J. Reine Angew. Math. **92**, 156 (1881)
55. K.L. Johnson, K. Kendall, A.D. Roberts, Proc. R. Soc. Lond. A **324**, 302 (1971)
56. J.N. Israelachvili, *Intermolecular and Surface Forces* (Academic, London, 1991)
57. F.I. Niordson, *Shell Theory* (North Holland, New York, 1985)
58. The factor $\frac{1}{2}$ is conventional. See also Ref. [57]
59. M. Tanemura, T. Ogawa, N. Ogita, J. Comp. Phys. **51**, 191 (1983)
60. J. M. Augenbaum, C.S. Peskin, J. Comp. Phys. **59**, 171 (1985)
61. A. Baumgärtner, J.-S. Ho, Phys. Rev. A **41**, 5747 (1989)
62. S. Komura, A. Baumgärtner, Phys. Rev. A **44**, 3511 (1991)
63. H.S. Seung, D.R. Nelson, Phys. Rev. A **38**, 1005 (1988)
64. Y. Kantor, D.R. Nelson, Phys. Rev. Lett. **58**, 2774 (1987)
65. Y. Kantor, D.R. Nelson, Phys. Rev. A **36**, 4024 (1987)
66. S.A. Safran, *Statistical Thermodynamics of Surface, Interfaces, and Membranes* (Addison-Wesley, New York, 1994)
67. W.H. Press, B.P. Flannery, S.A. Teukolsky, W.T. Vetterling, *Numerical Recipes* (Cambridge University, New York, 1989)
68. G. Gompper, D.M. Kroll, Phys. Rev. A **46**, 7466 (1992)
69. A.R. Bausch, M.J. Bowick, A. Cacciuto, A.D. Dinsmore, M.F. Hsu, D.R. Nelson, M.G. Nikolaides, A. Travesset, D.A. Weitz, Science **299**, 1716 (2003)
70. J. Lidmar, L. Mirny, D.R. Nelson, Phys. Rev. E **68**, 051910 (2003)
71. Y. Kantor, M. Kardar, D.R. Nelson, Phys. Rev. Lett. **57**, 791 (1986)
72. Y. Kantor, M. Kardar, D.R. Nelson, Phys. Rev. A **35**, 3056 (1987)
73. B. Roman, A. Pocheau, Europhys. Lett. **46**, 602 (1999)
74. Notice that the two-dimensional Young's modulus \hat{Y} (which is used in Ref. [63]) and the three-dimensional Young's modulus Y are related by $\hat{Y} = Yh$. Poisson's ratio is the same in the both dimensions
75. J. Tersoff, Phys. Rev. B **46**, 15546 (1992)
76. A. Fery (private communication)
77. T. Baumgart, S.T. Hess, W.W. Webb, Nature **425**, 821 (2003)
78. A. Hategan, R. Law, S. Kahn, D.E. Discher, Biophys. J. **85**, 2746 (2003)
79. A. Hategan, K. Sengupta, S. Kahn, E. Sackmann, D.E. Discher, Biophys. J. **87**, 3547 (2004)